

# A Mesh-Generation Scheme for the Large Helical Device Based on the Structure of Magnetic-Field Lines<sup>\*</sup>)

Daisuke TAKADA, Taku ITOH<sup>1)</sup>, Masahiro KOBAYASHI<sup>2)</sup> and Hiroaki NAKAMURA<sup>2,3)</sup>

*Graduate School of Industrial Technology, Nihon University, Narashino 275-8575, Japan*

<sup>1)</sup>*College of Industrial Technology, Nihon University, Narashino 275-8575, Japan*

<sup>2)</sup>*National Institute for Fusion Science, Toki 509-5292, Japan*

<sup>3)</sup>*Department of Electrical Engineering, Nagoya University, Nagoya 464-0813, Japan*

(Received 30 November 2020 / Accepted 12 February 2021)

We report herein an automated scheme for generating a mesh based on a structure of magnetic-field lines. For all angles in the toroidal subdomain, the mesh generated by this scheme must not contain broken tetragons. To satisfy this requirement, we propose herein a first method to detect broken elements and a second method to automatically modify the broken elements. We use the proposed mesh-generation scheme with magnetic-field data acquired on the magnetic axis of the Large Helical Device at  $R_{ax} = 3.75$  m. The results show that broken elements are detected by the first method, and the second method transforms broken elements into regular elements.

© 2021 The Japan Society of Plasma Science and Nuclear Fusion Research

Keywords: automatic mesh generation, tracing magnetic field line, detection of broken element, Large Helical Device, toroidal subdomain

DOI: 10.1585/pfr.16.2401086

## 1. Introduction

In magnetized plasma, plasma transport along magnetic-field lines becomes several orders of magnitude larger than cross-field transport. As a result, any mesh for plasma-transport simulations must be generated based on the magnetic-field structure to guarantee a clear separation between the parallel and the cross-field (perpendicular) transport. The three-dimensional (3D) edge plasma-transport code EMC3 uses a field-line-aligned 3D grid, whereby the computation domain is divided into several subdomains, and field-line mapping (or reversible field-line mapping) accurately connects the field-line coordinates between subdomains [1]. However, for EMC3-EIRENE [2], which has been implemented for transport analysis in the Large Helical Device (LHD) [3–5], the 3D grid is generated for each toroidal subdomain based mainly on the following time-consuming manual procedure that takes into account the 3D magnetic-field structure.

1. Determine the initial toroidal angle  $\phi = \phi_0$ .
2. Generate an initial mesh on the  $R$ - $Z$  plane for  $\phi = \phi_0$ . Note that all nodes of the mesh become initial positions for magnetic-field lines.
3. Trace all magnetic-field lines corresponding to the nodes to the next angle  $\phi_{k+1} = \phi_k + \Delta\phi$  ( $k = 0, 1, \dots$ ) until reaching the last angle. Note that the mesh structure retains the initial indices given at  $\phi = \phi_0$ , so that each tetragon is reconstructed at the new  $\phi$ .

author's e-mail: cida19009@g.nihon-u.ac.jp, itoh.taku@nihon-u.ac.jp

<sup>\*</sup>) This article is based on the presentation at the 29th International Toki Conference on Plasma and Fusion Research (ITC29).

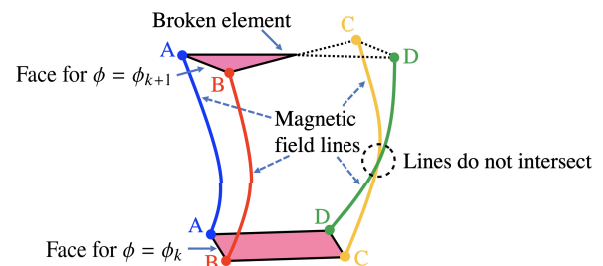


Fig. 1 Schematic illustration of a broken element. Yellow and green lines are twisted between element faces for  $\phi = \phi_k$  and  $\phi_{k+1}$ .

In step 3 of this procedure, given that the indices are retained for all angles, some tetragons in the mesh break due to strong magnetic shear at the edge region, as shown in Fig. 1 (see Section 4 for definition of a broken element). In this case, the mesh generation process starts again from step 2. Note that the initial mesh in this process must differ from the previous mesh. Since determining new positions for nodes that do not break elements until final angle in the toroidal subdomain is difficult, the restart process is not launched automatically; instead, the positions of nodes for constructing the new initial mesh are determined manually.

The purpose of the present work is to develop an automated mesh-generation scheme that produces unbroken tetragons for all angles in the toroidal subdomain. Toward this end, we propose a first method for detecting broken elements and a second method to automatically modify the broken elements.

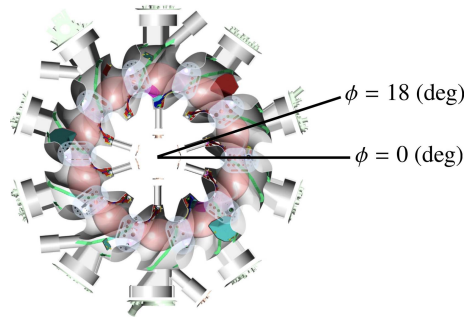


Fig. 2 Schematic illustration of toroidal subdomain in the LHD.

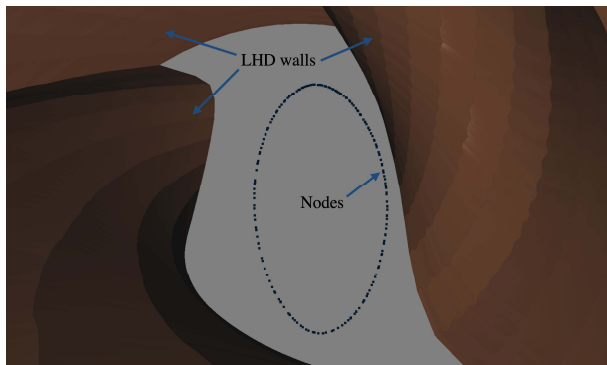


Fig. 3 Nodes of an almost ellipsoidal shape on the plane for initial angle  $\phi_0 = 0^\circ$ .

## 2. Problem Settings

We consider generating a mesh based on the structure of the magnetic-field lines. This section presents the problem settings.

### 2.1 Toroidal subdomain in LHD

We define a region contained in  $\phi \in [0^\circ, 18^\circ]$  as a toroidal subdomain in the LHD (see Fig. 2, where  $\phi$  is the toroidal angle from step 1 in of the mesh-generation procedure in Section 1. In addition, we define the initial angle  $\phi_0 = 0^\circ$ , and the last angle  $\phi_{\max} = 18^\circ$ .

The magnetic field in the LHD is created by two helical coils and by additional poloidal coils surrounding a confined plasma [6]. This magnetic field is calculated and stored in a regular spatial grid, typically with 5 mm steps in  $R$  and  $Z$  directions. The data consist of  $R_i(m)$ ,  $\phi_j(\text{deg})$ ,  $Z_k(m)$ , and  $\mathbf{B}_{ijk} = [B_r^{ijk}, B_\phi^{ijk}, B_z^{ijk}]^T(\text{T})$ , where  $R_i$ ,  $\phi_j$ , and  $Z_k$  are the coordinates in a cylindrical coordinate system  $(R, \phi, Z)$ , and  $\mathbf{B}_{ijk}$  is the magnetic field at  $(R_i, \phi_j, Z_k)$ . In the data, the step sizes for  $R_i$ ,  $\phi_j$  and  $Z_k$  are 5 mm,  $0.25^\circ$ , and 5 mm, respectively. We also assume that the magnetic-field strength  $\mathbf{B}$  can be obtained at any point within the toroidal subdomain by interpolating adjacent  $\mathbf{B}_{ijk}$ .

### 2.2 Initial mesh

In the plane for the initial angle  $\phi_0$ , we align nodes in an approximate ellipsoidal contour, as shown in Fig. 3.

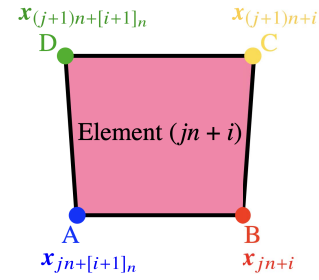


Fig. 4 Schematic view of element  $(jn + i)$ .

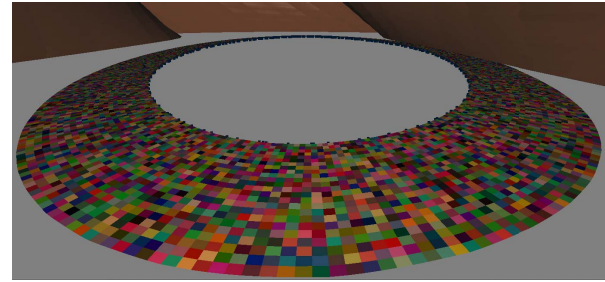


Fig. 5 Initial mesh for the case where  $a = \ell = 5 \text{ mm}$  and  $L = 24$ .

Given the stochastization of the magnetic field near the edge of the LHD, the magnetic surface is not smooth. To generate an initial mesh, a smooth magnetic surface is created by applying a spline scheme to smooth the original data. Then initial nodes  $\mathcal{X}_{\text{ini}} = \{\mathbf{x}_0, \mathbf{x}_1, \dots, \mathbf{x}_{n-1}\}$  are obtained by interpolation, so that  $|\mathbf{x}_i - \mathbf{x}_{[i+1]_n}|$  ( $i = 0, 1, \dots, n-1$ ) are almost the same length  $\ell$ , where  $[i+1]_n$  is the remainder of  $i+1$  modulo the number  $n$  of initial nodes.

From the initial nodes  $\mathcal{X}_{\text{ini}}$ , we obtain an exact ellipsoid by applying a least-squares fitting. To extend the grid radially outward, additional nodes are created along outward normals  $\mathcal{N} = \{\mathbf{n}_0, \mathbf{n}_1, \dots, \mathbf{n}_{n-1}\}$  emanating from the initial nodes. This is done because the normals obtained from the exact ellipsoid do not intersect with each other. Although the outward normals can be calculated from the interpolation by applying a spline, they sometimes intersect with each other. Given that the normals are used to generate nodes for the initial mesh, they must not intersect.

The initial mesh consists of nodes  $\mathbf{x}_{jn+i} = \mathbf{x}_i + a j \mathbf{n}_i$  ( $i = 0, 1, \dots, n-1$ ,  $j = 0, 1, \dots, L$ ), where  $a$  is a parameter, and  $L$  is the number of layers in the initial mesh. For nodes  $\mathcal{X} = \{\mathbf{x}_0, \mathbf{x}_1, \dots, \mathbf{x}_{N-1}\}$ , element  $(jn + i)$  of the initial mesh is constructed as a tetragon ABCD that consists of  $\{\mathbf{x}_{jn+[i+1]_n}, \mathbf{x}_{jn+i}, \mathbf{x}_{(j+1)n+i}, \mathbf{x}_{(j+1)n+[i+1]_n}\}$ , where  $N = n(L+1)$ . As shown in Fig. 4, the vertices A, B, C and D correspond to  $\mathbf{x}_{jn+[i+1]_n}$ ,  $\mathbf{x}_{jn+i}$ ,  $\mathbf{x}_{(j+1)n+i}$  and  $\mathbf{x}_{(j+1)n+[i+1]_n}$ , respectively. For the case where  $a = \ell = 5 \text{ mm}$  and  $L = 24$ , the initial mesh is shown in Fig. 5. In this figure, the elements are randomly colored. Note that we do not generate the mesh inside of the ellipsoid, since EMC3-EIRENE is employed to simulate the peripheral plasma of the LHD.

### 3. Tracing Magnetic-Field Lines

All nodes  $\mathcal{X}$  are on the  $R$ - $Z$  plane for  $\phi = \phi_0$ , and the magnetic field lines are traced from these nodes. The magnetic-field lines on the  $R$ - $Z$  plane are determined sequentially for  $\phi_k = k\Delta\phi$  ( $k = 1, 2, \dots, n_\phi$ ) by solving the following equations, where  $n_\phi$  is the division number for the  $\phi$ -direction.

$$\frac{dr}{d\phi} = r \frac{B_r}{B_\phi}, \tag{1}$$

$$\frac{dz}{d\phi} = r \frac{B_z}{B_\phi}. \tag{2}$$

To solve (1) and (2), we use the fourth-order Runge-Kutta method for the first three steps, and the fourth-order Adams-Bashforth-Moulton method for the remaining steps.

As shown in Fig. 6, layer numbers are assigned sequentially from the inside, and the node numbers are assigned sequentially counterclockwise from the inside. The number for a given element is given by the lower-right node number of the element (i.e., the node number of vertex B in Fig. 4).

To generate a mesh, the mesh of layer zero is first generated for  $\phi_k = k\Delta\phi$  ( $k = 1, 2, \dots, n_\phi$ ); that is, after finishing the procedure of layer zero, layer 1 is started. The process is similar for layer 2 and grater. For layer  $j$ , magnetic-field lines start from nodes constructing element  $jn$ , in ascending order. Thus, in Fig. 6, the red dots are the starting points for each layer, and the elements are generated along the red arrows by tracing magnetic-field lines. The traces are repeated until  $\phi = \phi_{\max} = n_\phi\Delta\phi$  in the same layer. After generating all the elements in a given layer, the process moves to the next layer (see blue arrows in Fig. 6).

In this process, the mesh structure retains the previous angle; that is, the node indices for constructing each element in the mesh are the same for all angles. For this reason, some of the tetragon elements contained in the mesh are broken, as shown in Fig. 1. Thus, the mesh-generation process must detect broken elements. This is done in the following C-like pseudo-code for mesh generation:

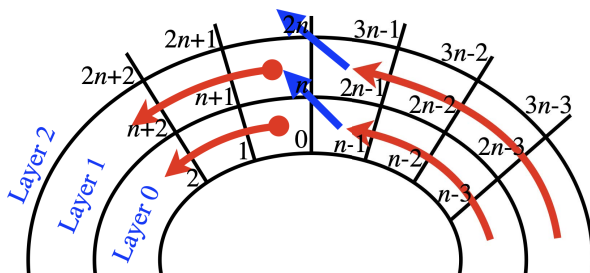


Fig. 6 Schematic diagram showing order in which mesh is generated.

```

for(j = 0; j < N; j++){
    s_j = 0; // step number for node j
}
Δφ = (π(φ_max - φ_min)/180)/n_φ; // φ_min = 0, φ_max = 18
for(j = 0; j < L; j++){
    for(k = 0; k < n_φ; k++){
        for(i = 0; i < n; i++){
            trace(jn + [i + 1]_n, k); // for vertex A
            trace(jn + i, k); // for vertex B
            trace((j + 1)n + i, k); // for vertex C
            trace((j + 1)n + [i + 1]_n, k); // for vertex D
            detection(k, jn + [i + 1]_n, jn + i,
                (j + 1)n + i, (j + 1)n + [i + 1]_n);
        }
    }
}
}

trace(j, k){
    if(s_j ≤ k && s_j < n_φ) {
        The magnetic field line corresponding to x_j is traced
        to next angle φ_{k+1} = φ_k + Δφ, by solving (1) and (2).
        ++s_j;
    }
}

detection(k, A, B, C, D){
    Broken elements are detected by using p = x_D^{(k)} - x_A^{(k)}
    and q = x_C^{(k)} - x_B^{(k)} (see Section 4).
}

```

### 4. Detecting Broken Elements

Let  $\mathcal{X}^{(k)} = \{\mathbf{x}_1^{(k)}, \mathbf{x}_2^{(k)}, \dots, \mathbf{x}_{N-1}^{(k)}\}$  be the nodes on plane  $R$ - $Z$  for  $\phi = \phi_k$ . Note that  $\mathcal{X}^{(0)} = \mathcal{X}$ . Here,  $\mathbf{x}_j^{(k)}$  is the coordinate of the magnetic-field line corresponding to  $\mathbf{x}_j$ .

This section proposes a strategy for detecting broken elements. Toward this end, we first consider straight lines  $\hat{p}(\alpha)$  and  $\hat{q}(\beta)$  in 3D as follows:

$$\hat{p}(\alpha) = \mathbf{p}_0 + \alpha \mathbf{s}, \tag{3}$$

$$\hat{q}(\beta) = \mathbf{q}_0 + \beta \mathbf{t}, \tag{4}$$

where  $\mathbf{p}_0$  and  $\mathbf{q}_0$  are the starting positions of  $\hat{p}(\alpha)$  and  $\hat{q}(\beta)$ , respectively, and  $\mathbf{s}$  and  $\mathbf{t}$  are different unit vectors. If  $\alpha$  and  $\beta$  satisfy

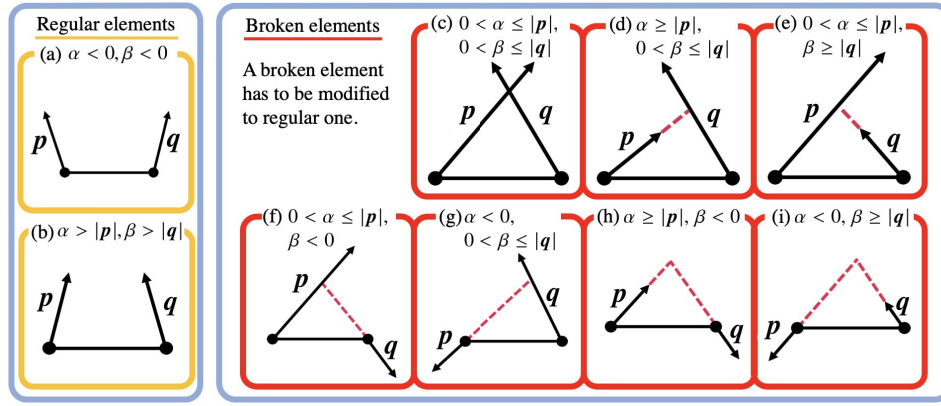
$$\hat{p}(\alpha) - \hat{q}(\beta) = \mathbf{0}, \tag{5}$$

then  $\hat{p}(\alpha)$  and  $\hat{q}(\beta)$  intersect. However, in general,  $\hat{p}(\alpha)$  and  $\hat{q}(\beta)$  are skew lines. For this reason, we now consider determining  $\alpha$  and  $\beta$  by minimizing the distance between the tips of  $\hat{p}(\alpha)$  and  $\hat{q}(\beta)$ .

When  $\hat{p}(\alpha)$  and  $\hat{q}(\beta)$  are projected onto plane  $\mathbf{s}$ - $\mathbf{t}$ ,  $\hat{p}(\alpha) - \hat{q}(\beta)$  must be parallel to  $\mathbf{s} \times \mathbf{t}$  if the tips of  $\hat{p}(\alpha)$  and  $\hat{q}(\beta)$  coincide. Thus,

$$(\mathbf{s} \times \mathbf{t}) \cdot ((\hat{p}(\alpha) - \hat{q}(\beta)) \times \mathbf{s}) = 0, \tag{6}$$

$$(\mathbf{s} \times \mathbf{t}) \cdot ((\hat{p}(\alpha) - \hat{q}(\beta)) \times \mathbf{t}) = 0, \tag{7}$$


 Fig. 7 Element types (a)–(i) distinguished by  $\alpha$  and  $\beta$ .

are satisfied. Using (3), (4), (6) and (7),  $\alpha$  and  $\beta$  are given by

$$\alpha = -\frac{(\mathbf{s} \times \mathbf{t}) \cdot ((\mathbf{p}_0 - \mathbf{q}_0) \times \mathbf{t})}{(\mathbf{s} \times \mathbf{t}) \cdot (\mathbf{s} \times \mathbf{t})}, \quad (8)$$

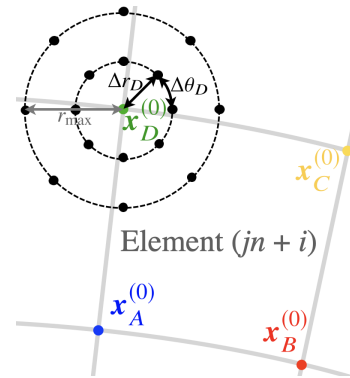
$$\beta = -\frac{(\mathbf{s} \times \mathbf{t}) \cdot ((\mathbf{p}_0 - \mathbf{q}_0) \times \mathbf{s})}{(\mathbf{s} \times \mathbf{t}) \cdot (\mathbf{s} \times \mathbf{t})}. \quad (9)$$

where,  $\mathbf{p} = \mathbf{x}_D^{(k)} - \mathbf{x}_A^{(k)} (= \overrightarrow{AD})$  and  $\mathbf{q} = \mathbf{x}_C^{(k)} - \mathbf{x}_B^{(k)} (= \overrightarrow{BC})$ . If  $\mathbf{p}_0 = \mathbf{x}_A^{(k)}$ ,  $\mathbf{s} = \mathbf{p}/|\mathbf{p}|$ ,  $\mathbf{q}_0 = \mathbf{x}_B^{(k)}$  and  $\mathbf{t} = \mathbf{q}/|\mathbf{q}|$  in each element,  $\hat{\mathbf{p}}(\alpha)$  and  $\hat{\mathbf{q}}(\beta)$  are on the  $R$ - $Z$  plane for  $\phi = \phi_k$ . In this case,  $\alpha$  and  $\beta$  satisfy (5). The values of  $\alpha$  and  $\beta$  are calculated by using (8) and (9), and the elements can be distinguished as types (a)–(i) in Fig. 7. Note that we define convex tetragons as regular elements. In addition, we define as broken elements not only tetragons with crossing sides but also tetragons with a vertex whose inner angle is greater than or equal to  $\pi$ . If broken elements are detected, they must be transformed into regular elements.

## 5. Automatic Mesh Modification

This section proposes a method for automatic mesh modification for broken elements. When executing the process for layer  $j$  ( $j = 1, 2, \dots, L-1$ ), we assume that elements generated by the mesh-generation process for layer  $(j-1)$  are not broken (i.e., vertices A and B are always normally positioned in all elements). For layer zero, we assume that nodes  $\{\mathbf{x}_0^{(k)}, \mathbf{x}_1^{(k)}, \dots, \mathbf{x}_{n-1}^{(k)}\}$  ( $k = 0, 1, \dots, n_\phi$ ) can be generated normally, since they are the innermost nodes and are almost certainly not broken in the mesh-generation process.

When element  $(jn+i)$  (i.e., element  $i$  of layer  $j$ ) breaks for  $\phi = \phi_k$ , the nodes  $\mathbf{x}_D^{(K)}$  ( $K = 0, 1, \dots, k$ ) are regenerated. This is because generating new nodes along an appropriate magnetic-field line is required in the modification process. Note that the modification of element  $(jn+i)$  may also be done by regenerating nodes  $\mathbf{x}_C^{(K)}$  ( $K = 0, 1, \dots, k$ ) of element  $(jn+i)$ . However, we do not regenerate them, since they also belong to element  $(jn+i-1)$ , which is not broken (we thus avoid reconstructing unbroken elements). Thus, this strategy only modifies nodes  $\mathbf{x}_D^{(K)}$  ( $K = 0, 1, \dots, k$ ).


 Fig. 8 New nodes around  $\mathbf{x}_D^{(0)}$ .

To modify  $\mathbf{x}_D^{(K)}$  ( $K = 0, 1, \dots, k$ ), we generate new nodes around  $\mathbf{x}_D^{(0)}$  on the  $R$ - $Z$  plane for  $\phi = \phi_0$ . For example, new nodes are circularly generated, as shown in Fig. 8. In this figure, the maximum radius  $r_{\max} < \min(a, \ell)$  (i.e.,  $r_{\max}$  is smaller than the minimum edge length of the element). To minimize changes to the element shape,  $r_{\max} \leq 0.5 \min(a, \ell)$  is recommended. In Fig. 8,  $\Delta r_D = r_{\max}/n_r$  and  $\Delta \theta_D = 2\pi/n_\theta$ , where  $n_r$  and  $n_\theta$  are the division numbers for the directions  $r$  and  $\theta$ , respectively.

The new nodes are generated in order of proximity to  $\mathbf{x}_D^{(0)}$ . Every time a new node  $\hat{\mathbf{x}}_D^{(0)}$  is generated, we trace the corresponding magnetic-field line until  $\phi = \phi_k$ , that is,  $\hat{\mathbf{x}}_D^{(K)}$  ( $K = 1, 2, \dots, k$ ) are determined by solving (1) and (2). While the tracing process,  $\mathbf{x}_D^{(K)} = \hat{\mathbf{x}}_D^{(K)}$  are assumed, and the strategy for detecting broken elements is applied to elements  $(jn+i)$  and  $(jn+i+1)$  for  $\phi = \phi_k$ . This is because their shapes change by  $\mathbf{x}_D^{(K)} = \hat{\mathbf{x}}_D^{(K)}$ . Note that element  $(jn+i+1)$  for  $\phi = \phi_k$  is not yet generated (see C-like pseudo-code in Section 3).

For all angles  $\phi = \phi_K$  ( $K = 1, 2, \dots, k$ ), if elements  $(jn+i)$  and  $(jn+i+1)$  are not broken,  $\mathbf{x}_D^{(K)} = \hat{\mathbf{x}}_D^{(K)}$  ( $K = 1, 2, \dots, k$ ) are formally set, and the modification process terminates successfully. If a broken element is detected during tracing, the trace exits immediately, and the next new node  $\hat{\mathbf{x}}_D^{(0)}$  is generated. After that, a new tracing pro-

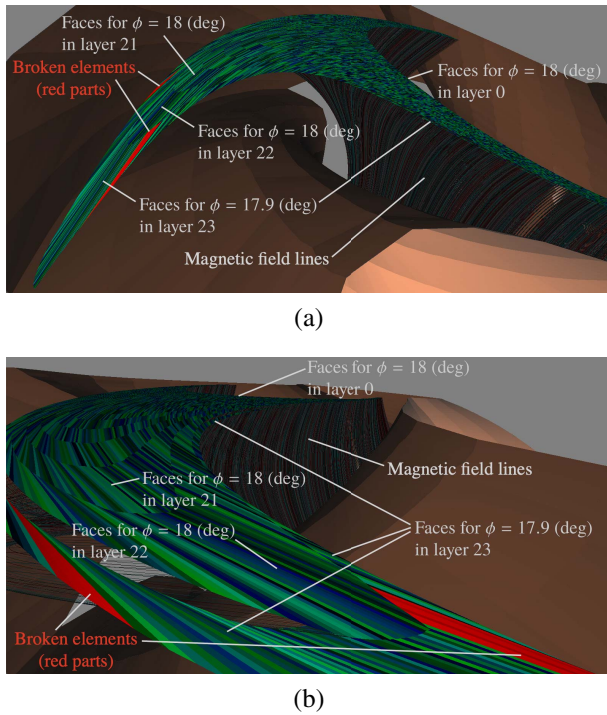


Fig. 9 (a) Result of mesh generation for  $k = 179$  ( $\phi = 17.9^\circ$ ) in layer 23, and (b) another perspective of the same result. The red parts are detected as broken elements (The red parts are already modified by the strategy described in Section 5). Both panels show the magnetic-field lines and faces for  $\phi = 18^\circ$  in layers 0–22.

cess starts. The modification process continues until successful termination, following which the mesh-generation procedure continues from element  $(jn + i + 1)$  for  $\phi = \phi_k$ .

## 6. Examples

In this section, we apply the mesh-generation scheme that includes detecting broken elements and automatic mesh modification. The parameters are set as  $n = 778$ ,  $L = 24$ ,  $a = \ell = 5$  mm,  $n_\phi = 180$ ,  $r_{\max} = 0.5\ell$ ,  $n_r = 32$ , and  $n_\theta = 128$ . To generate an initial mesh, we use the nodes from Fig. 3, and the initial mesh generated is shown in Fig. 5. The mesh is generated in the toroidal subdomain for  $\phi = [0^\circ, 18^\circ]$ , and  $\phi_0 = 0^\circ$ . The present analysis uses the magnetic-field configuration of  $R_{\text{ax}} = 3.75$  m, where  $R_{\text{ax}}$  is a magnetic axis position.

Figure 9 (a) shows a mesh generation result for  $k = 179$  ( $\phi = 17.9^\circ$ ) in layer 23. The outermost mesh is the result. Figure 9 (b) shows another perspective of the same result. Figure 9 also shows the mesh generated for  $k = 180$  ( $\phi = 18^\circ$ ) in layers 0–22 and the magnetic-field lines obtained by solving (1) and (2). Although mesh generation produces all elements, only elements in the left half of the initial mesh in Fig. 5 are updated; those in the right half remain unchanged with respect to the initial mesh. This is because only the elements in the left half change significantly. Thus, we focus on the elements in the left half of the initial mesh.

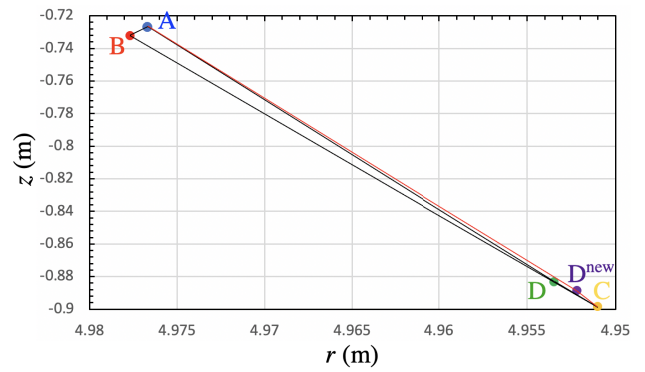


Fig. 10 Result of modifying element 18624 for  $k = 180$  ( $\phi = 18^\circ$ ). This element is detected as type (c).

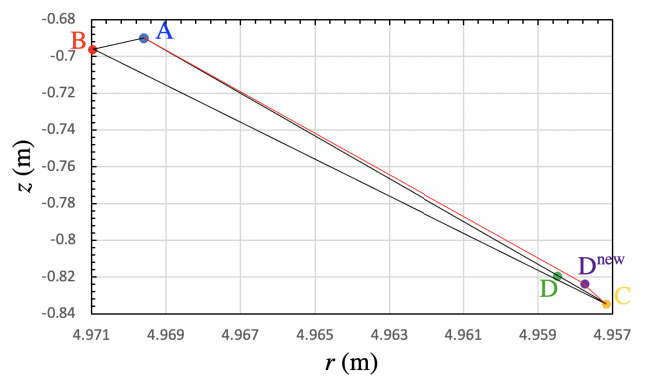


Fig. 11 Result of modifying element 18630 for  $k = 180$  ( $\phi = 18^\circ$ ). This element is detected as type (d).

Figures 9 (a) and 9 (b) show regular elements in green and blue based colors, which reveal that many elements for  $\phi = 17.9^\circ$  and  $18^\circ$  are longer than those for  $\phi = 0^\circ$  shown in Fig. 5. This is because the magnetic-field strength changes considerably. Depending on the structure of magnetic-field lines, broken elements sometimes appear. The method described in Section 4 detects the red parts as broken elements. Note that these broken elements are automatically modified by the method described in Section 5. The red parts in Figs. 9 (a) and 9 (b) are already modified by the method of Section 5.

For  $k = 180$  ( $\phi = 18^\circ$ ) in layer 23, some elements are detected as broken. Figures 10 and 11 show the results of each type of modification, which appear at elements 18624 and 18630, respectively. Elements 18624 and 18630 are detected as types (c) and (d), respectively, as shown in Fig. 7. In Figs. 10 and 11,  $D^{\text{new}}$  denotes the new nodes generated by the method of automatic modification of elements. In these figures, new edges appear as red lines. These results show that tetragons are constructed by generating  $D^{\text{new}}$ , which leads to the conclusion that, in this case, broken elements are detected and automatically modified by the methods detailed in Sections 4 and 5.

## 7. Conclusion

To construct an automated scheme for generating a mesh based on the structure of magnetic-field lines, we propose herein two strategies for detecting broken elements and automatically repairing them. A mesh-generation scheme based on these strategies has been applied to a magnetic-field data acquired along the magnetic axis at  $R_{ax} = 3.75$  m. The results lead to the following conclusions:

1. Broken elements can be detected as described in Section 4.
2. Broken elements can be automatically transformed into regular elements as described in Section 5.

Although broken elements can be modified by the proposed method, the elements remain thin tetragons, as shown in Figs. 10 and 11. Even if a broken element can be modified to a regular shape, the modified element may be excessively thin. In future work, we will therefore investigate techniques to detect excessively thin structures.

In addition, the mesh-generation scheme proposed

herein does not consider the magnetic-field strength in the algorithm. Thus, the fineness of the initial mesh is nearly identical over the whole region. In practice, the mesh should be finer in regions of greater magnetic-field strength. In future work, we will therefore develop a mesh-generation scheme that considers the magnetic-field strength.

## Acknowledgment

This work was partially supported by JSPS KAKENHI Grant Number JP18K11329. In addition, this work was supported in part by NIFS Collaboration Research Program (NIFS20KNTS068).

- [1] Y. Feng and F. Sardei, *Phys. Plasmas* **12**, 052505 (2005).
- [2] Y. Feng *et al.*, *Contrib. Plasma Phys.* **54**, 426 (2014).
- [3] S. Dai *et al.*, *Nucl. Fusion* **56**, 066005 (2016).
- [4] G. Kawamura *et al.*, *Contrib. Plasma Phys.* **54**, 437 (2014).
- [5] M. Kobayashi *et al.*, *Nucl. Fusion* **53**, 033011 (2013).
- [6] N. Ohya *et al.*, *Nucl. Fusion* **34**, 387 (1994).